



Size-Dependent Fracture Characteristics of Intermetallic Alloys

Arun Raina¹

Received: 10 August 2021 / Accepted: 17 February 2022 / Published online: 4 April 2022
© The Author(s) 2022

Abstract

Background Lightweight alloys such as intermetallic titanium aluminide (TiAl) alloys are poised to be a potential candidate for replacing heavier nickel based super alloys in an aero engine. However, before an industry wide implementation is possible, it is indispensable to develop physically accurate computational material models which account for essential deformation and fracture mechanisms. This assists the virtual prototyping required for the new product development using TiAl components.

Objective The objective of this work is to determine the effect of size of tested specimens on their fracture energy and provide a physically motivated scaling law.

Methods In this work, the quasi-brittle behavior of TiAl alloys is experimentally and numerically investigated. A total number of 29 geometrically identical TiAl specimens of three different sizes are tested in a three-point bending setup. Since the final abrupt failure of each specimen is preceded by plasticity, a theoretical and numerical framework which accounts for both elastic and plastic work densities is applied in simulations.

Results The fracture energy density for each tested size is calculated numerically which is found to be lower for larger volumes, thereby, confirming the size effect in intermetallic TiAl alloys. A novel size effect law is proposed which is based on two physically motivated coefficients.

Conclusions The work concludes with the quantitative knowledge of the size-dependent fracture energy of intermetallic alloys and an empirical scaling law to predict the same. Excellent predictive capability of the proposed law is successfully established with data of various quasi-brittle materials from literature.

Keywords Size effect · Fracture energy · Ductile fracture · Intermetallics · Phase field fracture

Introduction

Demanding engineering applications involve high strength metallic alloys or composites which guarantee a certain lifetime under usual (harsh) operating conditions [1, 2]. Often the components involved in such applications have complicated geometries which differ greatly from those geometries tested in labs to obtain material properties for design and analysis [3]. For example, blades or vanes in gas turbines or gearboxes in automobiles have geometries which render them difficult to test in labs. In addition, it is challenging to test the material response under realistic (operational)

multiphysical loads, which consist of combined mechanical, thermal and chemical (corrosion), on a test bench inside a lab. Furthermore, the material parameters deducted from conventional approach of material testing often assume isotropic and statistically homogeneous microstructure. Therefore, those parameters that drive the design and analysis of components with complicated geometries under complex loading conditions lead to conservative designs which must be addressed [4, 5].

Intermetallics, such as titanium aluminide (TiAl) alloys offer a compromise between metals and ceramics where some toughness can be sacrificed in favour of improved resistance to high temperature and oxidation and increased hardness, besides excellent strength-to-weight ratio. Of particular interest are γ -titanium aluminide (γ -TiAl) alloys which have attractive advantages for aerospace applications [6]. For aluminium content exceeding ≈ 53 at.%, γ -TiAl can solidify as a single phase alloy, which suffers from poor

✉ Arun Raina
arunraina@icloud.com

¹ German Aerospace Center (DLR e.V.), Institute of Test and Simulation for Gas Turbines, Am Technologiezentrum 5, Augsburg 86159, Germany



ductility and low fracture toughness at room temperature [7]. An improvement in the ductility and fracture toughness at room temperature is achieved in the two phase alloy consisting of γ -TiAl (face-centered tetragonal $L1_0$ structure) and α_2 -Ti₃Al (hexagonal DO_{19} structure) [8]. These duplex γ -TiAl based alloys can be used in the low pressure and low temperature (700°C) sections of an aero engine (gas turbine). The specific strength and stiffness of TiAl alloys with a density of 3.7–3.9 g·cm⁻³ is comparable to that of Nickel based super alloys with 8.5–9.0 g·cm⁻³ density [7]. It was shown in Yao and Marek [9] that oxidation in TiAl alloys in presence of sodium chloride deposits starts at 650°C, which is around expected operating conditions of TiAl components.

The current understanding of TiAl alloys is based on many years of research and development with the first patent in Blackburn and Smith [10]. However, the first commercial use in aviation industry happened in 2012 and as of 2014, 100,000 TiAl turbine blades had been installed on 500 GENx engines accruing 2.5 million hours in service without failure [11]. Nevertheless, certain aspects of deformation and failure mechanisms still remain unexplored leading to reluctance in industry-wide adaptation of TiAl alloys. In this work, one such attempt is undertaken to investigate the size-dependent fracture characteristics of quasi-brittle intermetallic alloys.

The statistical size effect in brittle materials was first theoretically described by the classical weakest link theory of Weibull [12] which postulated a distribution of structural strength as a function of volume. However, Bažant [13] showed that the Weibull theory was not able to describe failure in quasi-brittle engineering materials such as concretes where the structure failure occurs after a long stable crack growth. A deterministic size effect law was proposed with the nominal material strength (usually flexural stress at failure) as a function of a characteristic length of the structure. A more recent review of literature covering size effect theories in quasi-brittle materials can be found in [14]. Quasi-brittle materials (e.g. reinforced concrete, rocks, tough ceramics, fibre-reinforced composites, fatigue-embrittled steel, ferritic steels at low temperature) are those materials where failure is caused by (i) fracture rather than plastic yield and (ii) the crack tip is surrounded by a fracture process zone (FPZ) in which progressive distributed damage takes place which is smaller compared to the specimen dimensions [15]. In contrast, the FPZ in brittle materials is non-existent and the post-peak response shows sudden drop to zero load.

Despite extensive research in the size-dependent failure characteristics of quasi-brittle concrete, literature does not seem to have a common consensus of underlying mechanics [16, 17]. The size effect laws proposed by Bažant and co-workers [13, 15] defined two types of laws: type 1 law applicable to smooth specimens without notches and type

2 law applicable to specimens with notches. Within type 2 law, two different empirical equations are proposed to deal with shallow and deep notches separately. Thereby, introducing three equations to characterize the size-dependent behavior of a quasi-brittle material. On the other hand, it is argued by Hu and co-workers [16, 18] that all types of notch lengths can be characterized by a unique empirical law, referred to as boundary effect model, without resorting to extensive parameter fitting for each notch size. A concept of fictitious- and equivalent crack length was introduced in the latter to predict size-dependent fracture characteristics

The size effect in metals is generally studied in the context of “Hall-Petch effect” [19, 20] – so called *smaller is stronger* – where the yield strength is observed to be inversely proportional to the grain size. The strengthening is understood to be a result of lower stresses at the tip of dislocation pile-up which in turn requires higher applied stress to generate further dislocations [21].

Fleck et al. [22] showed that the size effect in copper wires is due to the accumulation of geometrically necessary dislocations which scales with the gradient of plastic strains. In Tsuchiya et al. [23], thin films made of polycrystalline silicon were tested with different sizes. It was observed that the mean tensile strength depended on the specimen length and generally reduced with increasing length. Wallin [24] analyzed vast amounts of fracture toughness data of nuclear grade pressure vessel steel to demonstrate the size effect phenomena with the master curve analysis. The tests were performed at a wide range of temperatures and the size effect was found to be more prominent in specimens undergoing cleavage fracture. Greer and De Hosson [25] provided a comprehensive overview of size effect phenomena at micro and nano scales in crystalline as well as amorphous solids.

The notch sensitivity in metals is also widely studied see e.g. [26–29]. It is understood that low strength metallic alloys are notch insensitive where as high strength alloys show notch sensitivity in fracture assessment. The effect of stress concentration due to a notch in conventional coarse-grained metals is diminished due to crack-tip plasticity and notch blunting [30]. However, in nano-crystalline or ultrafine grained metals, stress concentration effect due to a notch is dominant leading to notch sensitive strength [31]. Abnormal grain growth was observed ahead of a notch in [32] which led to earlier fracture with increasing notch radius. The review article in Berto and Lazzarin [33] presented a criterion based on an averaged strain energy density of a control volume ahead of a notch. The criterion provided a critical value for fracture assessment of brittle and quasi-brittle materials which is unique and independent of notch geometry.

Linear elastic fracture mechanics (LEFM) defines the critical energy release rate \mathcal{G}_c and the critical stress intensity factor K_{Ic} (plane strain mode I) as two fundamental



parameters which are indicative of the material fracture toughness [34]. These parameters are related as $K_{Ic}^2 = \mathcal{G}E'$ where $E' = E/(1 - \nu^2)$ for plane strain and $E' = E$ for plane stress. E and ν are Young’s modulus and Poisson’s ratio, respectively. This relation together with the Griffith energy balance [35] yields the critical flaw size – so called *transition flaw size* – in a material and is written as

$$a_T = K_{Ic}^2 / \pi \sigma_y^2 \tag{1}$$

where σ_y is the material yield strength which denotes the onset of plasticity. Contours of a_T over a wide range of K_{Ic} and σ_y are plotted in Fig. 1a. For very small flaws $a_T \rightarrow 0$, yielding precedes fracture, whereas for large flaws sudden fracture dominates. A schematic plot in Fig. 1b indicates a stress-based failure criterion. For flaw sizes $a < a_T$, design by strength is used where the critical stress σ_c has a threshold value of yield strength σ_y . For flaw sizes $a > a_T$, design by LEFM is used where the critical stress σ_c has a threshold which is a function of plane strain fracture toughness K_{Ic} with an $a^{-1/2}$ flaw size dependence. In this work, a failure criterion based on the fracture energy density w_c proposed in [36] is used to study the size effect phenomena. A schematic plot in Fig. 1c depicts the relation of the fracture energy density based criterion with the flaw size a . In the LEFM regime, w_c has a^{-1} flaw size dependence.

For the intermetallic TiAl alloy under consideration in this work, yielding is observed to precede sudden failure

in experiments. Therefore, for the analysis of data and to determine a suitable threshold for fracture, a theoretical and numerical framework which accurately accounts for crack propagation in materials undergoing plastic yielding is desirable. The computational modeling of fracture phenomena is a vast subject. For complete references and a detailed description of various seminal works present in literature on this subject, the reader is referred to the authors’ work in Raina [37] and Linder and Raina [38] on the modeling of strong discontinuities and the references cited therein. The reader is also referred to the work in Raina and Miehe [39] and Miehe et al. [36, 40], and the references cited therein, on the phase field modeling of fracture. In particular, results of Miehe et al. [36], where a gradient-extended plasticity-damage theory based on the phase field method of fracture was developed, are utilized in this work. The fracture energy density w_c based failure criterion accounts for elastic and plastic work densities to define variationally consistent driving forces for crack initiation and growth in a plastic medium. Thus, w_c as an accurate threshold for fracture is calculated in this work for the tested TiAl samples to postulate an empirical size effect law.

The outline of the rest of the paper is as follows. "Experimental Procedures" describes the experimental procedures adopted in this work for testing intermetallic TiAl alloys. "Phase Field Method for Ductile Fracture At Small Strains" summarizes the theoretical and numerical framework of phase field modeling of ductile fracture in small strain

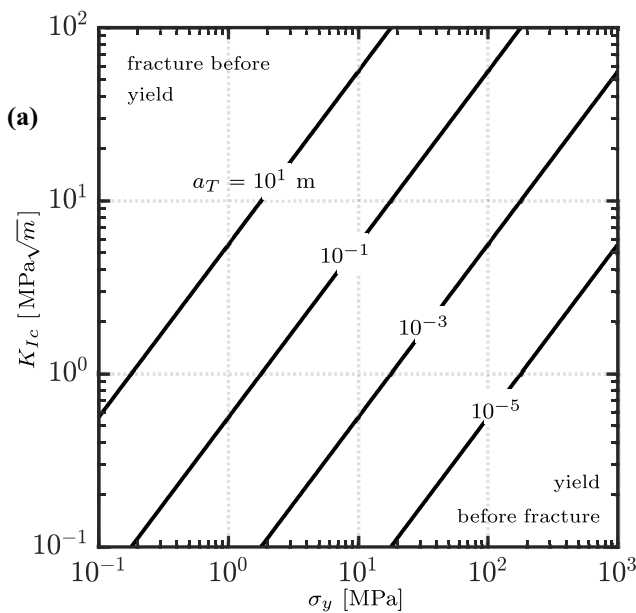
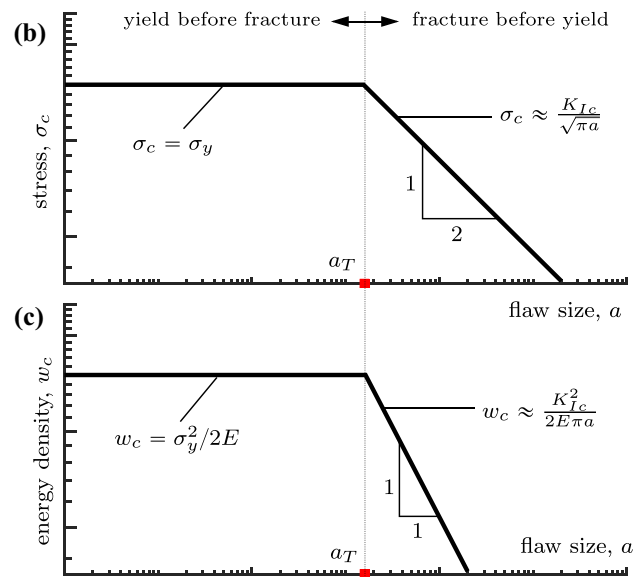


Fig. 1 (a) Contours of transition flaw size a_T from equation (1) over the parametric space of plane strain fracture toughness K_{Ic} and material yield strength σ_y . For very small a_T , yielding precedes fracture (typical of high strength alloys) and for very large a_T , sudden fracture without yielding is observed (typical of ceramics). Schematic illustration of (b) stress-based failure threshold and (c) energy density based failure threshold used in this work, both as a function of material flaw size a . For $a > a_T$, stress varies with $a^{-1/2}$ dependence whereas energy varies with a^{-1} dependence



tion of (b) stress-based failure threshold and (c) energy density based failure threshold used in this work, both as a function of material flaw size a . For $a > a_T$, stress varies with $a^{-1/2}$ dependence whereas energy varies with a^{-1} dependence



setting which is used for the analysis of experimental data. "Size Effect Analysis With Simulations of Three-Point Bending Experiments" presents the numerical simulation results and the analysis of experiments to calculate the fracture energy density of TiAl samples. A novel size effect law is proposed. In "Further Discussions On the Size Effect Law", further justification and validation of the proposed law is provided with available data from literature. The concluding discussion is presented in "Concluding Remarks".

Experimental Procedures

The section presents the experimental procedures undertaken in this work to obtain data for size effect analysis of metallic alloys.

TiAl as Intermetallic Alloy

Titanium aluminide of type GE48-2-2 with the constituents titanium (48 at%), aluminium (48 at%), chromium (2 at%) and niobium (2 at%) and chemical composition Ti-33Al-2.6Cr-4.8Nb (wt%) was selected for the experimental investigations in this work. TiAl GE48-2-2 remelt stocks were manufactured by single or double vacuum arc remelting (VAR) with consumable electrodes made of compacted titanium sponge, aluminium and master alloys. Hot isostatic pressing (HIP) and heat treatment was done to produce a duplex microstructure α_2 and γ grains. The heating rate during HIP was ca. 10 K/min while the cooling rate was a function of temperature and at the beginning lied around 15 K/min. The material was supplied by GfE Metalle und Materialien GmbH from Nürnberg Germany in the form of a cylindrical slug of diameter 80 mm and height 380 mm. The manufacturer provided density and hardness of the TiAl alloy was $3.97 \text{ g}\cdot\text{cm}^{-3}$ and 285 HV10, respectively.

Three-Point Bending Experiments

Beams of rectangular cross-section of height H , width W and length $L = 4.2H$ were cut from the slugs using the electrical discharge machining technique. This was done by first cutting slices of circular discs of thickness W from the cylindrical slug. From each such disc, specimens were finally cut with random orientations to avoid a preferential direction. A schematic illustration of the geometry and loading condition is shown in Fig. 2. Three geometrically identical sizes of height $H = [6, 9, 12]$ mm are selected and for each size 11, 14 and 4 specimens, respectively, are obtained. A statistically relevant scatter in data is captured for sizes $H = [6, 9]$ mm. However, due to fewer specimens for $H = 12$ mm, the scatter obtained may not be statistically relevant. The width $W = 6$ mm is fixed for all the specimens which ensures that

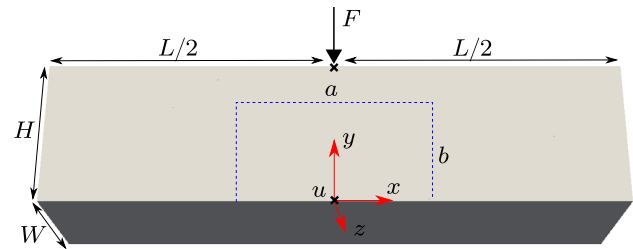


Fig. 2 An illustration of the three-point bending test setup. Force F at top center and deflection u at bottom center are measured for each test specimen. During simulations, displacement at $x = \pm L/2, y = 0$ is constrained along y - direction. Furthermore, to prevent rigid body motion, displacement at $x = -L/2, y = 0$ is additionally constrained along x, z - directions. A region of interest of size $a \times b \times W$ is shown which indicates the size of plastic domain at crack initiation (see Fig. 7)

crack propagation occurs in plane strain condition upon failure. The surface finish and dimensional tolerances follow the ASTM E 399-90 standard. Overall, 29 three-point bending experiments were performed in this work with a ZwickRoell Kappa 50 DS testing machine. The distance between the supporting pins of the test fixture was $4H$ and the diameter of the supporting pins was $H/2$. Depending upon the size of the specimen, the crosshead displacement rate ($\text{mm}\cdot\text{min}^{-1}$) of the test frame was adjusted to ensure a constant flexural strain rate of $5 \times 10^{-3} \text{ min}^{-1}$ for all tests. The experiments were performed at the mechanical testing facility of the University of Augsburg in Germany.

Force-Displacement Data

The displacements and strain distributions within the samples were captured with the digital image correlation (DIC) technique by using an Aramis™ system. The Aramis system composed of two digital cameras of 12 Megapixels resolution and OLED lightening connected to GOM Correlate software. The cameras were setup at a distance of 50 cm from specimens. To create a speckle pattern on tested specimens, white background was first sprayed at a pressure of 0.8 bar from a distance of 30 cm using a filter. It was followed by a point structure creation by spraying black paint at a pressure of 0.4 bar from a distance of 50 cm without a filter. The deflection u at the bottom center of each specimen was obtained from the DIC data. The load cell provided the force F at the top center of each specimen. The optical measurements were automatically started as soon as loading force F reached 5N. The force-displacement data of all the samples of each size $H = [6, 9, 12]$ mm are plotted in Fig. 3(a), (b) and (c), respectively. In Fig. 3(d), the mean force displacement of all samples H is plotted with a 95% confidence interval for force. Since the distribution family of data is unknown at



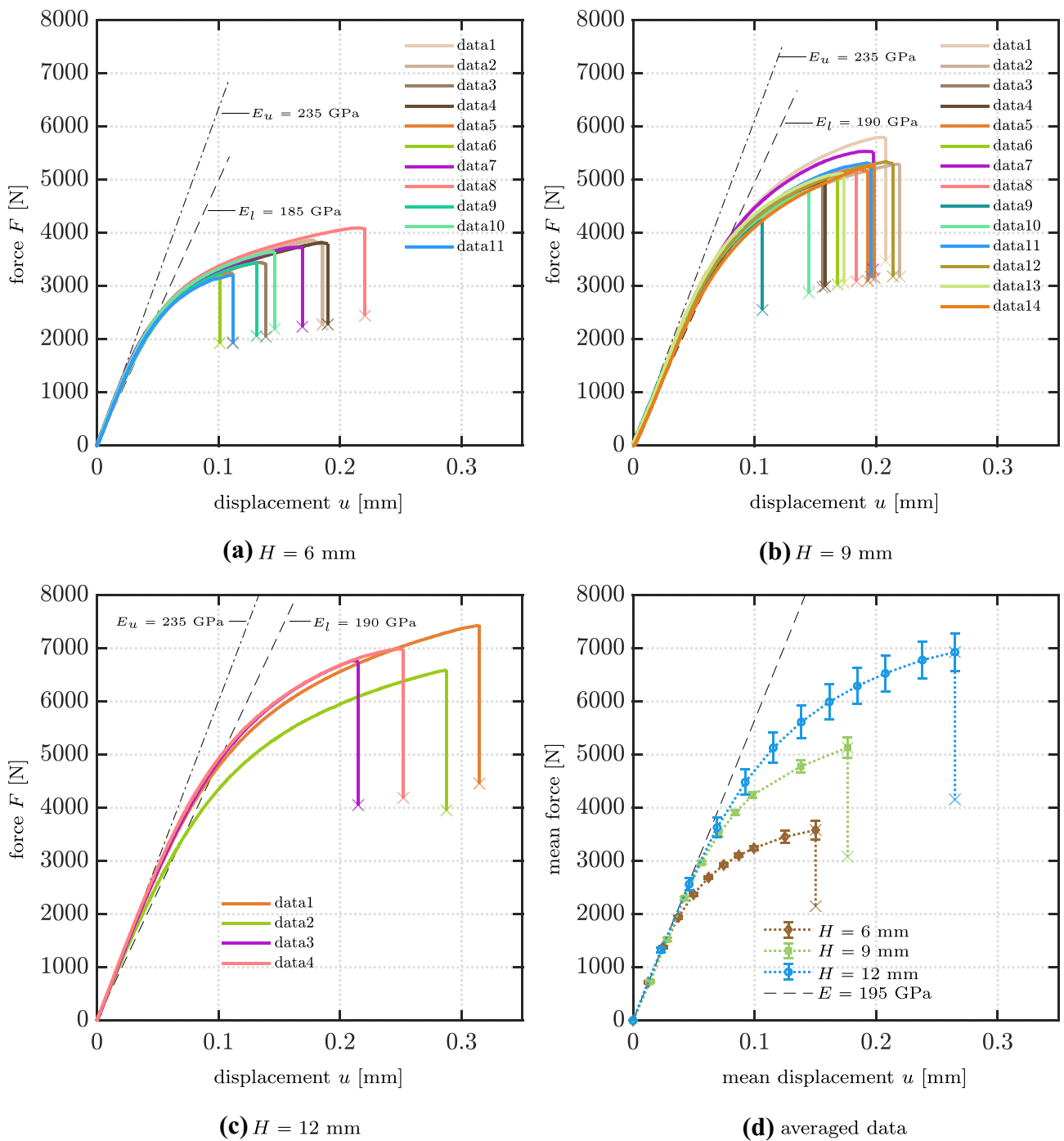


Fig. 3 Force-displacement data of three-point bending tests for (a) 11 samples of size $H = 6$ mm, (b) 14 samples of size $H = 9$ mm, and (c) 4 samples of size $H = 12$ mm. The scatter in elastic modulus for all three sizes is shown with lower (E_l) and upper (E_u) bound in each plot

(a–c). (d) The mean force-displacement data with 95% confidence interval for all three sizes are shown together which have an elastic modulus of $E = 195$ GPa

this stage, confidence intervals are calculated using the bootstrap algorithm of Matlab. The averaged responses are eventually used in "Size Effect Analysis With Simulations of Three-Point Bending Experiments" for calculating the fracture energy densities for each size. Based on the

data of all tested samples for each size H , the following observations are made.

- Scatter in the elasticity modulus (E): Full three-dimensional finite element simulations of three-point bending tests



were performed to obtain the lower ($E_l = 185\text{--}190$ GPa) and upper ($E_u = 235$ GPa) bounds of E in each size. These bounds were approximately 15% higher than the analytically obtained bounds with $u = FL^3/48EI + FLH^2/40GI$.

- A significant scatter in the maximum force (or maximum flexural stress). The average maximum force in $H = 6$ mm size is 3582 N, in $H = 9$ mm size is 5135 N and in $H = 12$ mm size is 6929 N. Confidence interval at maximum load for each size is approximately 10% of the average maximum force.
- A significant scatter in the maximum displacement (or maximum flexural strain). The average maximum displacement for $H = 6$ mm size is 0.154 mm, for $H = 9$ mm size is 0.179 mm and for $H = 12$ mm size is 0.267 mm. The width of confidence intervals (not plotted) for each $H = 6, 9, 12$ mm are approximately 30%, 18% and 30% of the corresponding average maximum displacements, respectively.
- All tested samples for each size H show considerable nonlinear behavior before final unstable crack growth and failure. The nonlinear behavior is attributed to plastic yielding due to ordinary dislocations, superdislocations and mechanical twinning [8].

Phase Field Method for Ductile Fracture At Small Strains

In this section, a summary of the theoretical and numerical developments in Miehe et al. [36] will be presented. Fourth order tensor fields are represented by four indices in the symbol subscript $(\cdot)_{ijkl}$, second order tensor fields by double indices $(\cdot)_{ij}$, vector fields by a single index $(\cdot)_i$ and scalar fields without an index. Unless otherwise stated, indices take the values from 1 to 3.

Introduction to Primary Field Variables

The primary field variables whose solution is sought are the displacement field $u_i : \mathcal{B} \times \mathcal{T} \rightarrow \mathbb{R}^3$ and the crack phase field $d : \mathcal{B} \times \mathcal{T} \rightarrow [0, 1]$ in a body $\mathcal{B} \subset \mathbb{R}^3$ at a material point $x_i \in \mathcal{B}$ and time $t \in \mathcal{T}$. The body \mathcal{B} is subjected to a volumetric body force $b_i : \mathcal{B} \rightarrow \mathbb{R}^3$, a Dirichlet boundary condition $u_0 : \partial_u \mathcal{B} \rightarrow \mathbb{R}^3$ and a traction boundary condition $t_0 : \partial_t \mathcal{B} \rightarrow \mathbb{R}^3$. The domain boundary $\partial \mathcal{B}$ is split into displacement $\partial_u \mathcal{B}$ and traction boundaries $\partial_t \mathcal{B}$ such that $\partial_u \mathcal{B} \cup \partial_t \mathcal{B} = \partial \mathcal{B}$ and $\partial_u \mathcal{B} \cap \partial_t \mathcal{B} = \emptyset$.

Denote $\varepsilon_{ij} = (\partial u_i / \partial x_j + \partial u_j / \partial x_i) / 2$ as the infinitesimal symmetric strain tensor and σ_{ij} the corresponding symmetric stress tensor in body \mathcal{B} . Consider an additive decomposition of the total strain tensor ε_{ij} into an elastic part ε_{ij}^e and a plastic part ε_{ij}^p as

$$\varepsilon_{ij}^e = \varepsilon_{ij} - \varepsilon_{ij}^p. \tag{2}$$

The kinematic decomposition (2) allows a definition of the free energy function dependent separately on elastic and plastic work contributions as shown later in "Formulation of Work Energies for Ductile Fracture". Furthermore, to model work hardening phenomena an equivalent plastic strain α is introduced as an internal variable by an evolution equation

$$\dot{\alpha} = \sqrt{\frac{2}{3}} \dot{\varepsilon}_{ij}^p \quad \text{with} \quad \dot{\alpha} \geq 0, \tag{3}$$

with the initial condition $\alpha(x_i, t = 0) = 0$.

The crack phase field d is introduced which allows regularization of sharp crack discontinuities. The crack phase field $d = 1$ characterizes a completely broken state and $d = 0$ a completely unbroken state. See Fig. 4 for an illustration. A crack surface functional Γ_l is introduced as

$$\Gamma_l(d) = \int_{\mathcal{B}} \gamma(d, \nabla d) dV, \tag{4}$$

in terms of a crack surface density function $\gamma(d, \nabla d)$ written as

$$\gamma(d, \nabla d) = \frac{1}{2l} (d^2 + l^2 |\nabla d|^2), \tag{5}$$

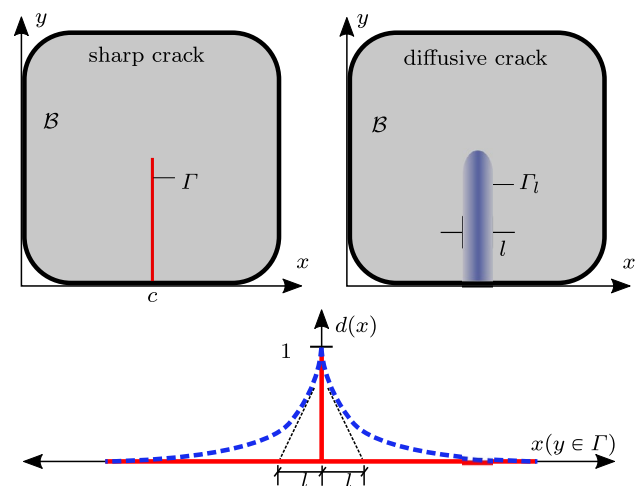


Fig. 4 A body \mathcal{B} with a sharp crack Γ (red) and a diffusive crack Γ_l (bluish) smeared over width l at $x = c$ are depicted on top left and right, respectively. The immediate numerical implication of sharp crack vs diffusive crack is a strong discontinuity in the displacement field vs a smoothly continuous displacement field. Bottom: a schematic plot of an auxiliary field variable d for a sharp crack (red) and a diffusive crack (dotted blue). $d = 1$ if $x = c$ otherwise 0 for a sharp crack $\forall y \in \Gamma$ where as $d = \exp[-|x|/l]$ for a diffusive crack satisfying $d = 1$ at $x = c \forall y \in \Gamma_l$. Parameter l represents the length scale of the phase field fracture



which depends on the crack phase field d and its spatial gradient ∇d and the length scale l . The phase field fracture length scale parameter l governs the regularization where a sharp crack topology is obtained in the limit of $l \rightarrow 0$ in the sense of Γ -convergence. The function $\gamma(d, \nabla d)$ plays an important role in the definition of the total work density of an elastoplastic solid undergoing ductile fracture. The minimization of crack surface functional (4) subject to Dirichlet-type constraints $\{d|d(x_i, t) = 1 \text{ at } x_i \in \Gamma(t)\}$ yields the crack phase field $d(x_i, t) \in \mathcal{B}$ for a given sharp crack surface topology $\Gamma(t)$ inside body \mathcal{B} . See Miehe et al. [36] for more details.

Formulation of Work Energies for Ductile Fracture

Let w_0^e be the elastic energy density of the unbroken part responsible for energy storage mechanisms which depends on ϵ_{ij}^e . Furthermore, let w_0^p be the dissipative plastic work density of the unbroken part which depends on α . Next, introduce the *critical fracture energy density* w_c which represents the work¹ needed for creating regularized crack surfaces in body \mathcal{B} . The work density (energy per unit volume) needed to deform an elastoplastic body element until fracture is written as [36]

$$W(\epsilon_{ij}^e, \alpha, d, \nabla d) = g(d)[w_0^e(\epsilon_{ij}^e) + w_0^p(\alpha)] + (1 - g(d))w_c + 2l\gamma(d, \nabla d)w_c. \tag{6}$$

A degradation function $g(d)$ is introduced in equation (6) which ensures the smooth transition of elastic-plastic work density ($w_0^e + w_0^p$) towards the critical fracture energy density w_c . A degradation function of quadratic form $g(d) = (1 - d)^2$ is considered which satisfies the constraints $g(0) = 1, g(1) = 0, g'(1) = 0$ and $g'(d) \leq 0$. A cubic degradation function satisfying the above constraints was proposed in [41].

For numerical simulations presented later in "Size Effect Analysis With Simulations of Three-Point Bending Experiments", the elastic work density w_0^e which represents a linear elastic isotropic response and is additively decomposed into volumetric and deviatoric parts is written as

$$w_0^e(\epsilon_{ij}^e) = (\kappa/2)\epsilon_{ii}^e\epsilon_{ii}^e + \mu\bar{\epsilon}_{ij}^e\bar{\epsilon}_{ji}^e. \tag{7}$$

The volumetric part is specified by the bulk modulus $\kappa > 0$ and the volumetric elastic strain ϵ_{ii}^e and the deviatoric part is specified by the shear modulus $\mu > 0$ and the deviatoric elastic strain $\bar{\epsilon}_{ij}^e$.

The dissipative plastic work density w_0^p used in simulations presented in "Size Effect Analysis With Simulations of Three-Point Bending Experiments" is written as

$$w_0^p(\alpha) = \sigma_y\alpha + (\sigma_\infty - \sigma_y)[\alpha + e^{(-\beta\alpha)}/\beta] + h\alpha^2/2 - (\sigma_\infty - \sigma_y)/\beta, \tag{8}$$

where $\sigma_y > 0$ is the yield strength, $\sigma_\infty \geq \sigma_y$ is the saturation yield strength, h is the isotropic hardening modulus and β is an exponent controlling the degree of nonlinear hardening. In Miehe et al. [36], (8) is shown to be a function of gradient of equivalent plastic strain $\nabla\alpha$, which is not considered in this work.

Furthermore, to prescribe thermodynamically consistent rate form of the plastic strain $\dot{\epsilon}_{ij}^p$ an elastic domain \mathbb{E} is written as

$$\mathbb{E} := \{(\bar{\sigma}_{ij}, \tilde{\sigma}_y) | \phi(\bar{\sigma}_{ij}, \tilde{\sigma}_y) \leq 0\}. \tag{9}$$

The elastic domain \mathbb{E} defines a threshold for plastic deformation in terms of a von Mises type plastic yield function ϕ which is written as

$$\phi(\bar{\sigma}_{ij}, \tilde{\sigma}_y) = \sqrt{\bar{\sigma}_{ij}\bar{\sigma}_{ij}} - \sqrt{2/3}\tilde{\sigma}_y, \tag{10}$$

where $\tilde{\sigma}_y = g(d)\partial w_0^p/\partial\alpha$ is the yield stress describing the nonlinear hardening and $\bar{\sigma}_{ij} = g(d)\partial w_0^e/\partial\bar{\epsilon}_{ij}^e$ is the deviatoric stress tensor.

A thermodynamically consistent rate form of crack phase field \dot{d} is determined by the variational derivative $\delta_d W$ of equation (6) with the following Kuhn-Tucker type equations [42]

$$\dot{d} \geq 0, \quad -\delta_d W \leq 0, \quad \dot{d}[-\delta_d W] = 0. \tag{11}$$

Governing Balance Equations of Coupled Elastic-Plastic Fracture

The variationally consistent derivation of balance equations for gradient-extended ductile fracture based on the rate-type minimization principle of the multi-field problem is showed in Miehe et al. [36]. In this section, the governing partial differential equations for the two primary global unknown variables, the displacement field vector u_i and the crack phase field d are presented briefly. The local form of balance of linear momentum for a static case of interest here is written as

$$\partial\sigma_{ij}/\partial x_j + b_i = 0 \quad \text{in } \mathcal{B} \tag{12}$$

¹ The conventional LEFM parameter, referred to as critical strain energy release rate and usually denoted as \mathcal{G}_c , is a measure of fracture toughness of a linear material and is measured in units of energy per unit area [N·m⁻¹]. For nonlinear materials, parameter \mathcal{G}_c is replaced by J -integral, also measured in units of energy per unit area. In contrast, the fracture energy density w_c used in equation (6) is the energy required to create regularized crack surfaces in the entire body \mathcal{B} (linear or nonlinear) and therefore measured in units of energy per unit volume [N·m⁻²]. It can be shown that $\mathcal{G}_c = w_c \times (V/A)$ in the limit of phase field fracture length scale $l \rightarrow 0$ where V is the specimen volume and A is the crack surface area.



where $\sigma_{ij} = g(d)\partial w_0^e/\partial \varepsilon_{ij}^e$ is the full stress tensor and b_i are the body forces. The Dirichlet and Neumann boundary conditions required for the solution of equation (12) are presented in "Introduction to Primary Field Variables".

The partial differential equation for the evolution of crack phase field in \mathcal{B} is written as

$$(1-d)[w_0^e + w_0^p - w_c] - (d - l^2 \Delta d)[w_c] = 0 \quad (13)$$

where Δ is the Laplacian operator. Equation (13) can be recast into the form

$$(1-d)\mathcal{H} = d - l^2 \Delta d \quad \text{in } \mathcal{B}, \quad (14)$$

where \mathcal{H} denotes the maximum positive value of a dimensionless crack driving state function D as

$$\mathcal{H} = \max_{s \in [0,t]} D(x_i, s) \geq 0, \quad (15)$$

with the function $D(x_i, t)$ written as

$$D(x_i, t) = \left\langle \frac{w_0^{e+}}{w_c} + \frac{w_0^p}{w_c} - 1 \right\rangle. \quad (16)$$

The Macaulay brackets $\langle \cdot \rangle$ in equation (16) together with equation (15) ensure that the crack growth rate $\dot{d} \geq 0$, i.e., cracks do not heal during unloading. From equation (16), it can be seen that the fracture energy density w_c defines a threshold which is the sum of elastic (7) and plastic (8) work densities in a solid undergoing fracture. For example, area under the stress-strain curve of an elasto-plastic solid until peak load (tensile strength) defines the critical fracture energy density w_c .

Size Effect Analysis With Simulations of Three-Point Bending Experiments

The experimental results presented in "Experimental Procedures" will be analyzed with the finite element numerical simulations based on the theoretical formulations presented in "Phase Field Method for Ductile Fracture At Small Strains".

Simulation Setup and Results

Full three-dimensional simulations of the three-point bending tests described in "Three-Point Bending Experiments" are performed. The finite element program is implemented in parallel FEAP². The geometry and boundary conditions are shown in Fig. 2. The three sizes $H = [6, 9, 12]$ mm

are discretized with 864×10^3 , 1944×10^3 and 3456×10^3 regular linear hexahedral elements, respectively. The chosen discretization ensures a constant fracture length scale $l = 100 \mu\text{m}$ in all simulations which is required to make quantitative comparisons of results from different sizes. The selection of mesh size ($h_e \leq l/2$) is based on two considerations. First, as discussed in "Introduction to Primary Field Variables", the Γ -convergence of regularized crack surfaces to sharp cracks is achieved for $l \rightarrow 0$. Hence, a very small length scale l is a requirement in the phase field simulations to ensure that dissipation in regularized crack surfaces is of the same order as sharp cracks. Furthermore, considerations of the problem size and the required compute capacity necessitates a practical value of $l > 0$. Second, the chosen discretization is fine enough to avoid mesh sensitive results in the absence of gradient of equivalent plastic strain (6). A Dirichlet boundary condition is prescribed at the center of the top layer where $u_0 = 0.3 \text{ mm}$ is applied in time $T = 1 \text{ s}$ with $\Delta t := t_{n+1} - t_n = 10^{-3} \text{ s}$. Due to a large size of the problem, simulations are carried out with parallel computing on a DLR HPC cluster³. The material constants used in simulations are listed in Table 1. Note that μ and κ in equation (7) are defined in terms of E and ν for isotropic materials.

The summation of nodal reaction forces at the center of top layer and the deflection at the center of bottom layer is obtained as the simulation output for each time step. Convergence is achieved in 4-6 global Newton iterations in each time step. A comparison of the simulated force displacement results of sizes $H = [6, 9, 12]$ mm with their corresponding mean values from the experiments are plotted in Fig. 5(a). The mean forces from experimental results are plotted together with 95% confidence intervals. The simulated force displacement response is in good agreement with the experiment data. The simulations are stopped as soon as the force drops significantly after the crack initiation. Another form of validation of numerical results is shown in Fig. 6 where the flexural and transverse strain distributions from DIC data are compared with the simulations for $H = 6 \text{ mm}$ size. The strain distributions are compared at the time step just before crack initiation leading to sudden failure. Similar comparisons are observed for other specimen sizes. Overall, a high accuracy of simulation results is established in this work.

As shown in Table 1, the only material property that differs among the three tested sizes during simulations is the fracture energy density w_c . For example, w_c reduces by ca. 20% as the specimen size changes from $H = 6$ to 9 mm, i.e., volume increases by 125%. The observed trend is, however, not supported by size $H = 12 \text{ mm}$ which shows increase in w_c relative to size $H = 9 \text{ mm}$. It is concluded that due to fewer

² <http://projects.ce.berkeley.edu/feap>

³ <https://www.top500.org/system/179779/>



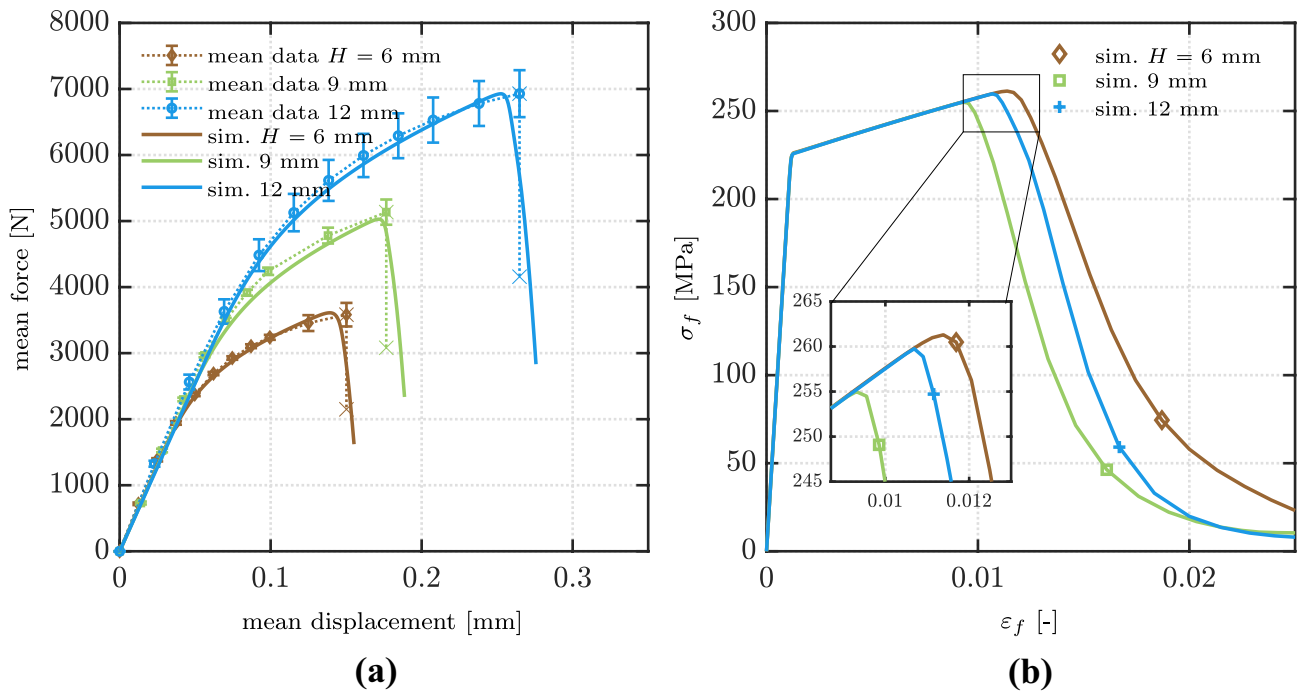


Fig. 5 (a) Comparison of simulated force displacement response for all three sizes $H = [6, 9, 12]$ mm with the mean force displacement data. The mean forces from data (Fig. 2) are plotted with the corre-

sponding 95% confidence intervals. (b) Simulated flexural stress σ_f versus flexural strain ϵ_f for all three sizes are plotted to highlight varying stress levels at failure

Table 1 Material parameters used in the simulations in "Size Effect Analysis With Simulations of Three-Point Bending Experiments". Note that the fracture energy density w_c is not constant for the three sizes $H = [6, 9, 12]$ mm tested in this work

E [GPa]	ν [-]	σ_y [MPa]	σ_∞ [MPa]	β [-]	h [MPa]	l [mm]	w_c [MPa]		
							$H = 6$	$H = 9$	$H = 12$
195	0.3	225	420	20	125	0.1	2.726	2.180	2.568

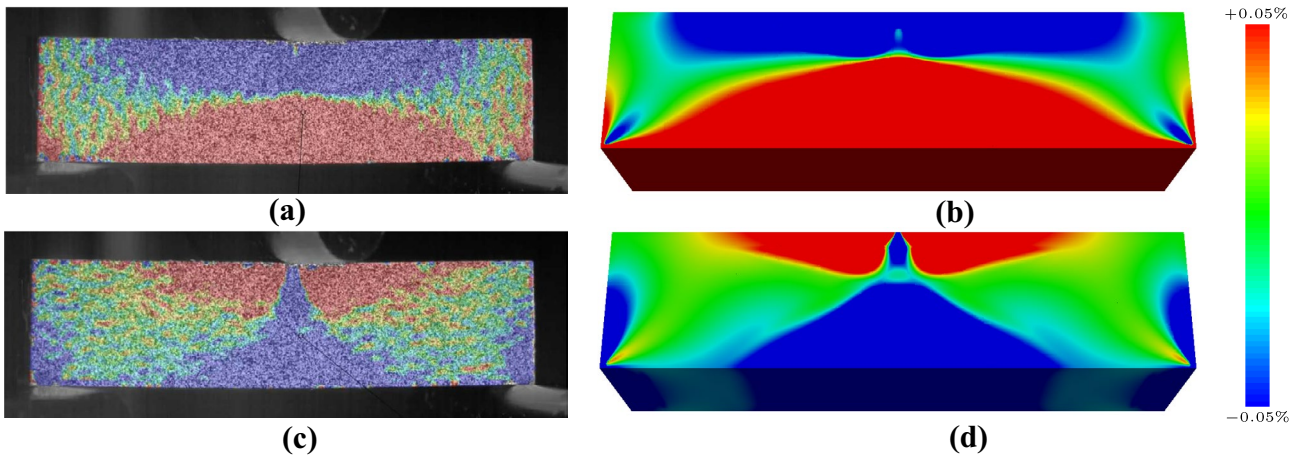


Fig. 6 For the size $H = 6$ mm, flexural strain data measured with (a) DIC and (b) finite element simulations. Similarly, transversal strain data measured with (c) DIC and (d) finite element simulations. The

strain distributions are plotted at the instance of time just before crack initiation leading to sudden failure. The color legend corresponds to both test and simulations



samples for $H = 12$ mm (total 4), the scatter is not statistically relevant and is skewed more towards higher w_c values.

Since the force displacement data from experiments shows nonlinear behaviour due to plasticity, the corresponding flexural stress σ_f versus flexural strain ϵ_f can only be plotted numerically, as shown in Fig. 5(b) for all sizes. These values are obtained at the bottom layer center (flexural) by taking an average of the field variables over the length $L/6$. It is to be emphasized here that the elastic behavior of the tested TiAl alloy holds only till very small flexural strain $\epsilon_f \approx 0.125\%$. The plasticity starts when the flexural stresses σ_f increase to σ_y with the eventual failure occurring at $\epsilon_f \approx 1\%$. As discussed in "Governing Balance Equations of Coupled Elastic-Plastic Fracture", the evolution of crack phase field d is governed by the corresponding elastic and plastic energy contributions (16) during loading.

Large Scale Yielding At Crack-Tip Initiation

The evaluation of fracture behavior of specimens with a single parameter such as \mathcal{G}_c or J -integral becomes invalid in large-scale yielding as those parameters exhibit size and geometry dependence [34]. In this work, based on the simulations of TiAl three-point bending tests, an attempt is made to establish the presence of large-scale yielding conditions in tests.

We borrow fundamental concepts from fracture mechanics. The strip-yield model of Dugdale [43] and Barenblatt [44] estimates the plastic zone size r_y ahead of a sharp crack tip in elastic-plastic solids under plane stress conditions as

$$r_y = (\pi/8)(K_{Ic}/\sigma_y)^2. \quad (17)$$

The plastic zone size (17) is similar to the second order estimate of Irwin [45]. However, size r_y holds in the limit of small-scale yielding, i.e., when r_y is much smaller than the notch and specimen dimensions. For our TiAl alloy, using

the manufacturer reported fracture toughness ($K_{Ic} = 15\text{--}18\text{MPa}\sqrt{m}$) and the evaluated yield strength ($\sigma_y = 225$ MPa), the estimated plastic zone size is $r_y = 1.75\text{--}2.5$ mm (in case of a hypothetical notched specimen). It is to be emphasized that the calculated r_y is only valid for a notched specimen and its purpose in the given three-point bending tests is merely to provide an estimation of a range of plastic zone size for small-scale yielding. Nonetheless, we show that the crack initiation and propagation in three-point bending occurs in fully yielded zone.

In Fig. 7(a), the amount of plastic yielding at the instant of crack initiation is depicted as equivalent plastic strain α distribution. The contours are obtained from the region of interest with size $a \times b \times W$ as shown in Fig. 2. For the size $H = 6$ mm, $a \approx 0.45L \approx 11$ mm and $b \approx 0.6H \approx 3.6$ mm. It can be established that the plastic yielding occurs over length scales greater than the estimated plastic zone size r_y (17) for small-scale yielding. A similar observation is made for other sizes. Hence, the crack initiation and growth is assumed to take place under large-scale yielding conditions which further justify the application of theory of ductile fracture presented in "Phase Field Methods for Ductile Fracture At Small Strains".

The simulated final crack growth pattern upon failure is shown in Fig. 7(b) as a distribution of the crack phase field variable d in the same region of interest as Fig. 7(a). It is to be noted here that all the tested TiAl specimens (Fig. 3) failed with a single unstable crack initiating from the bottom center and growing towards the top center. The simulated crack pattern arise from the shear localization occurring on planes with the highest shear stress due to ductile fracture criterion (16). Since the fracture energy density w_c listed in Table 1 correspond to a threshold before crack initiation, the final crack path pattern has no influence on the reported size effect. In fact, the problem presents an outlook for future enhancements of the current methodology to predict brittle type crack growth post yielding.

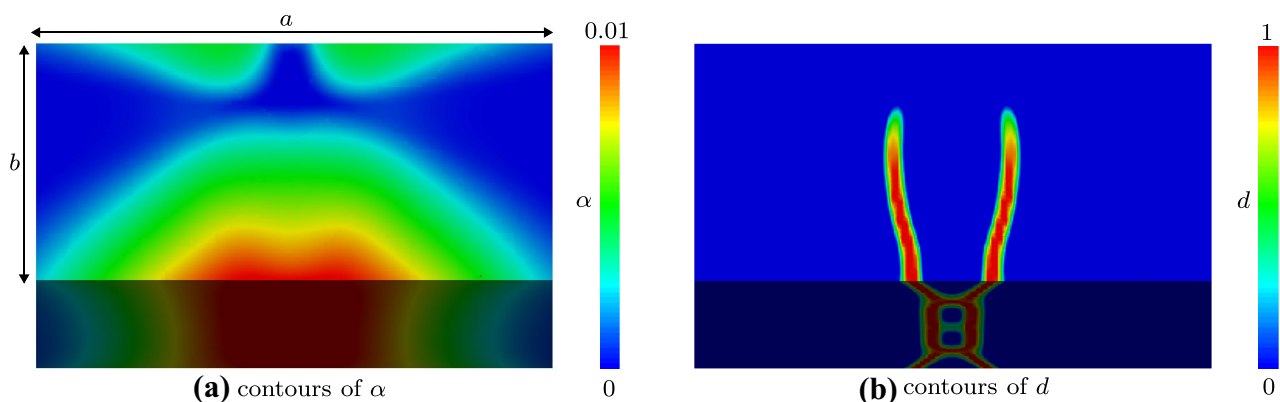


Fig. 7 Simulations results for size $H = 6$ mm within the region of interest $a \times b \times W$ shown in Fig. 2 where $a = 0.45L$ and $b = 0.6H$. (a) The distribution of equivalent plastic strain α just before crack ini-

tiation ($\alpha_c = 10.6 \times 10^{-3}$). (b) Contours of crack phase field d depicting the final fracture pattern during simulations



Proposed Empirical Size Effect Law

In "Introduction", the widely used theories for analyzing the size effect phenomena in quasi-brittle materials were introduced. Keeping in mind the aforementioned state-of-the-art regarding size effect laws, some key aspects are considered to be the most desirable of an empirical size effect law used in a constitutive model development. These aspects ensure successful implementation of such a model in the design and analysis of industrially relevant advanced applications and are listed as follows:

- **Simplicity of model:** The size effect law to be used in design and analysis is based on coefficients which are physically motivated. E.g., coefficients such as notch to height ratio of a specimen used in size effect laws in the aforementioned papers cannot be determined for complex geometries.
- **Efficiency of model:** The coefficients of an empirical size effect law can be obtained with fewer and simpler experiments without straining the resources. E.g., a size effect law which require more than two coefficients demands series of experiments and complex fitting procedures.
- **Predictive capability of model:** The empirical size effect law should be able to predict the material response under arbitrary loading and for arbitrary geometries.

To analyze the data of fracture energy density w_c of tested TiAl alloys shown in Table 1, a new size effect law is proposed in this work which relates the fracture energy density w_c with the absolute volume V of the specimen. Let $w_0 > 0$ be a reference fracture energy density corresponding to a reference volume $V_0 > 0$, the proposed size effect law takes the following form

$$w_c = \frac{2 w_0}{1 + (V/V_0)^{1/2}} \tag{18}$$

The proposed law (18) is bounded by two physical limits: a) $w_c \rightarrow 0$ when $V \rightarrow \infty$, and b) $w_c \rightarrow w_0$ when $V \rightarrow V_0$. As discussed in "Introduction", the influence of a notch size is not considered in equation (18) as material strength of metallic alloys is generally notch insensitive. This allows to maintain the simplicity and efficiency of the model.

Given the w_c and V data for the two tested sizes $H = [6, 9]$ mm of the given TiAl alloy, a linear regression analysis of equation (18) is performed and the results plotted in Fig. 8(a). The w_c value corresponding to each size H has a 95% confidence interval attached. It is to be emphasized here that the data of $H = 12$ mm is not considered in the linear regression analysis due to reasons mentioned in "Three-Point Bending Experiments". The estimated constants obtained from the linear regression are $w_0 = 2.76$ MPa

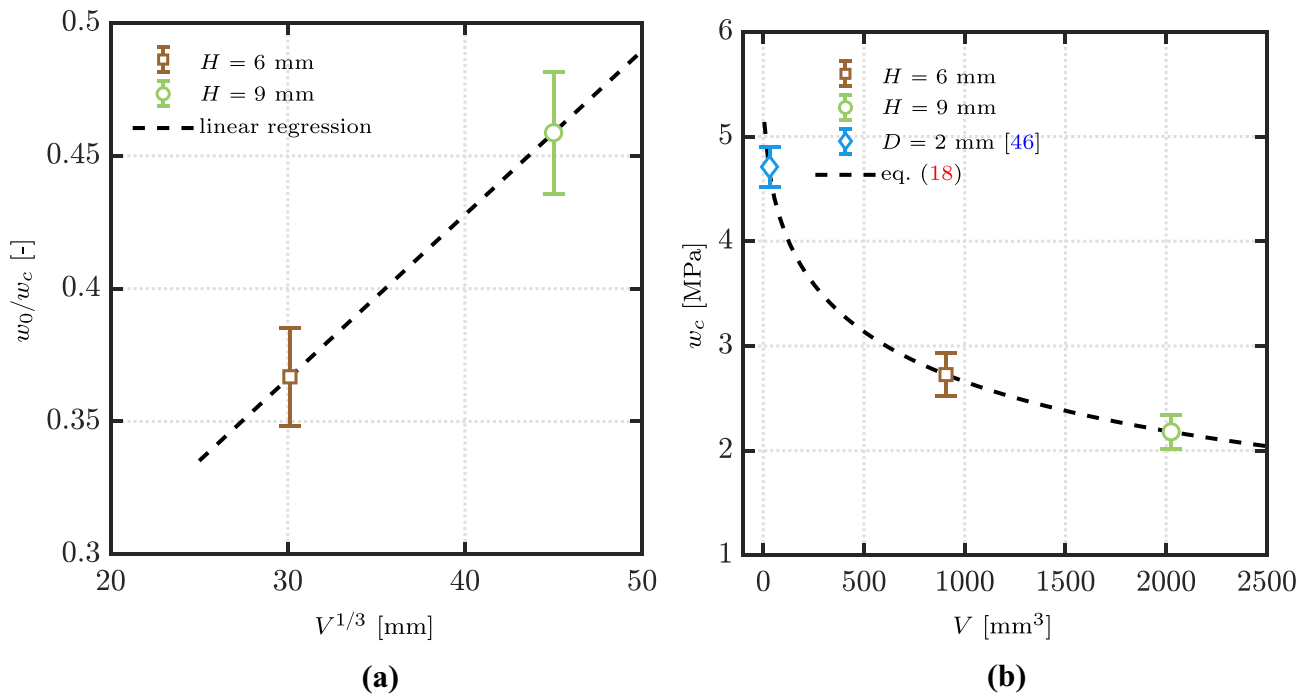


Fig. 8 Based on the w_c data of sizes $H = [6, 9]$ mm attached with 95% confidence interval **(a)** linear regression analysis of equation (18) estimates $w_0 = 2.76$ MPa and $V_0 = 856.97$ mm³ for the tested TiAl alloy, and **(b)** size effect law (18) with estimated w_0 and V_0 is plotted and shows smaller the volume tougher it becomes. The fracture

energy density w_c of $D = 2$ mm diameter TiAl rod from experiments in Dresbach et al. [46] is accurately predicted by the size effect law (18) with the derived coefficients from the tests performed in this work



and $V_0 = 856.97 \text{ mm}^3$. The size effect law (18) is plotted in Fig. 8(b) based on the estimated w_0 and V_0 values which confirms the physical relevance of equation (18), i.e., the smaller volume is tougher. The proposed size effect law (18) with the estimated coefficients w_0 and V_0 based on three-point bending tests in this work is able to accurately predict the fracture energy density of a 2 mm diameter TiAl rod obtained from tensile tests in [46]. Hence, clearly demonstrating the size-dependent fracture energy of intermetallic TiAl alloys on one hand as well as the excellent predictive capability of the proposed size effect mechanism on the other.

A theoretical background to the derivation of equation (18) with further application to different classes of quasi-brittle materials using the data from literature is shown in the next section.

Further Discussion On the Size Effect Law

Existing Size Effect Laws

A deterministic size effect law based on the crack band theory was proposed in [13]. It stated that stress redistribution in a narrow band ahead of a crack-tip releases strain energy during fracture. For deeply notched specimens, the nominal strength σ_N of a structure of size D can be written as

$$\sigma_N = B\sigma_y / (1 + D/D_0)^{1/2}, \quad (19)$$

where $B\sigma_y$ and D_0 are empirical coefficients which are estimated from a curve fitting exercise (linear regression) and depend upon the notch to specimen width ratio. The constants B and σ_y cannot be evaluated separately and are obtained from testing geometrically identical specimens which need to be recalculated each time the notch geometry is changed.

In [16], a boundary effect model was proposed based on the hypothesis of the interaction of FPZ with structure boundaries. An equation similar to equation (19) was proposed as

$$\sigma_N = \sigma_y / (1 + a/a_0)^{1/2}, \quad (20)$$

where a is the effective notch length which includes a fictitious crack growth and $a_0 = 0.25(K_{Ic}/\sigma_y)^2$ is a characteristic crack length. The relation (20) holds for specimens with and without notches and depends on fundamental material constants σ_y and K_{Ic} . The nominal strength σ_N used in equation (20) is understood as the strength of net cross-section.

The size effect laws (19)–(20) are derived based on the assumption of linear elastic behavior before fracture. By considering similar asymptotic series expansions as in Bažant [13] and the dimensional considerations $w_c \propto \sigma_N^2$, the new empirical law is proposed in equation (18) which is

not limited to linear elastic brittle fracture. The critical fracture energy density w_c consists of both the elastic and plastic work densities as shown in equation (16). It is to be noted that for linear elastic brittle solids, (18) is identical to equation (20) and requires fewer fitting parameters as demonstrated in "16". However, instead of defining the *brittleness number* as related to specimen dimension D/D_0 or crack length a/a_0 , the entire specimen volume V/V_0 is introduced in equation (18). As shown in [47], the essence of the weakest link theory applied to Weibull distribution [12] lies in the power law scaling with V/V_0 . Solids with larger volumes are more susceptible to failure where the probability of finding flaws of critical size is higher compared to smaller volumes. The excellent predictive capabilities of the proposed volume dependent size effect law (18) are presented in the following sections with data of various quasi-brittle materials from literature.

Validation with Hoover et al. (2013) Data

The predictability of equation (18) is tested with the data from Hoover et al. [48] which was obtained from the three-point bending tests of concrete material. Since all the specimens failed as linear elastic before fracture, the fracture energy density $w_c = \sigma_N^2/2E$ is obtained from the reported peak nominal stress σ_N and the concrete elastic modulus E .

Numerous geometrically identical specimens with four notch to width ratios $\alpha_i = [0, 0.075, 0.15, 0.3] \forall i = 1, 4$ were tested in [48] to study size effect⁴. For each α_i , the mean values of w_c corresponding to the tested volume V are plotted in Fig. 9. Since concrete behavior is notch-sensitive and the proposed size effect law (18) does not account for notch sensitivity, four sets of coefficients $\{w_0^i, V_0^i\}$ corresponding to each α_i are estimated. The prediction of size effect law (18) is also plotted in Fig. 9 which shows a very good agreement with the concrete data. The estimated coefficients w_0^i [MPa] and V_0^i [mm³] used in plotting Fig. 9 are $\{w_0^1 = 3.60 \times 10^{-4}, V_0^1 = 4.48 \times 10^7\}$, $\{w_0^2 = 2.91 \times 10^{-4}, V_0^2 = 3.35 \times 10^6\}$, $\{w_0^3 = 1.94 \times 10^{-4}, V_0^3 = 3.09 \times 10^6\}$, $\{w_0^4 = 0.95 \times 10^{-4}, V_0^4 = 2.05 \times 10^6\}$. It is once again emphasized here that the size effect law

⁴ A phase field method based approach for fracture in quasi-brittle materials was presented in Narayan and Anand [49] following the developments in Miehe et al. [36, 40]. Their numerical simulations of the three-point bending tests [48] could not predict the evident size effect shown in Fig. 9. Their phase field evolution equation setup (2.110) is different from the equations (14)–(16) used in this work. The authors used a critical threshold energy density ψ_{cr} equivalent to the fracture energy density w_c in this work. However, the authors introduced a new parameter ψ_* which controls the energy dissipation after crack initiation. From the reported values used in their simulations, $\psi_* \approx 4.5\psi_{cr}$.



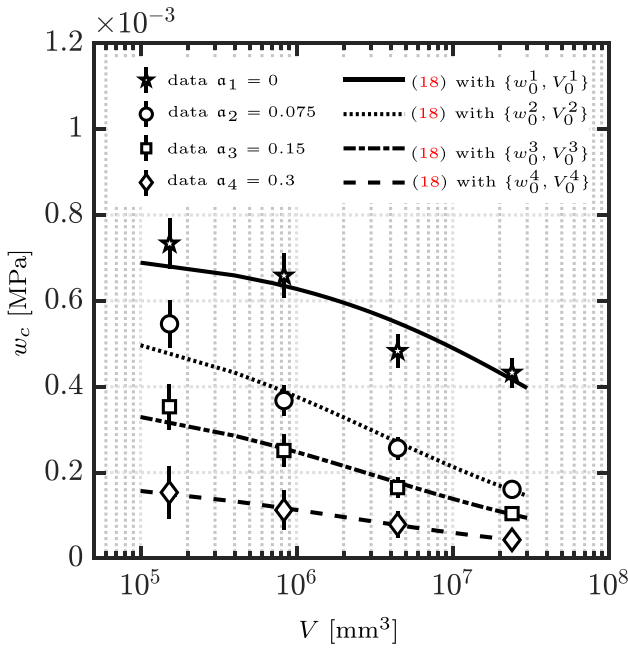


Fig. 9 Data of three-point bending tests of a concrete material from Hoover et al. [48] using four different notch to width ratios α_i . Predictions using size effect law (18) are superimposed, with different constants w_0 and V_0 evaluated for each α_i , show very good accuracy

for concretes proposed by Bažant and co-workers [13, 15] requires 12 parameters for geometries with $\alpha \leq 0.1$.

Validation with Wallin (2002) data

Compact tension test specimens of four different sizes made out of nuclear grade pressure vessel forging 22NiMoCr37 were tested in Wallin [24] at a wide range of temperatures from -154°C to $+20^\circ\text{C}$. The test specifications followed ESIS-P2 and ASTM E-1921 standards and thickness was varied as [12.5, 25, 50, 100] mm. J -integral values were measured for each of the 757 tests. To further validate the general applicability of the proposed law in equation (18), the test data at -91° of all the four sizes is selected from [24] where most of the specimens failed by cleavage fracture. Corresponding to each size, volume and J -integral values are retrieved for the validation process in this work. Since J -integral describes the energy released per unit surface area (similar to \mathcal{G}_c), it is transformed to the fracture energy density w_c (per unit volume) as

$$w_c = J \times \frac{\text{notch surface area}}{\text{specimen volume}} \tag{21}$$

See footnote (1) in "8". The plots in Fig. 10 show the calculated mean data of w_c with respective standard deviation

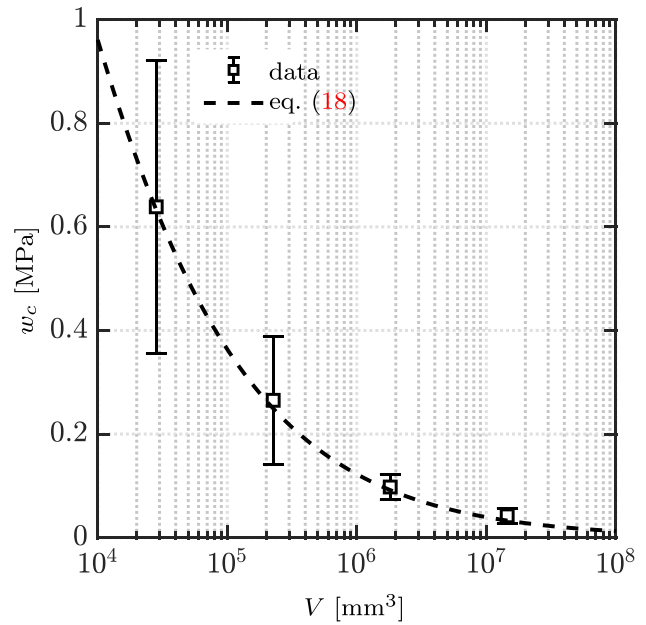


Fig. 10 Data of compact tension tests of different sizes performed with reactor pressure vessel alloy from [24]. The prediction with the proposed law (18) obtained with coefficients $w_0 = 2.0$ MPa and $V_0 = 1000$ mm^3 is superimposed

against the specimen volume V . The prediction with the proposed law (18) is also plotted using coefficients $w_0 = 2.0$ MPa and $V_0 = 1000$ mm^3 (the best fit). An excellent agreement with data confirms the applicability of relation (18) to metallic alloys other than intermetallics.

Validation with Tsuchiya et al. (2011) Data

Tsuchiya et al. [23] performed microscale tensile testing of smooth thin-films of polycrystalline silicon (poly-Si) to evaluate their reliability. Overall, six different sizes were tested each using two types of poly-Si: nondoped and P-doped. The validation of law (18) is performed with respect to the data of nondoped poly-Si in this work. The data in [23] provided maximum tensile strength σ_N and specimen dimensions for each of the six sizes. Due to brittle nature of failure of poly-Si thin films, fracture energy density $w_c = \sigma_N^2/2E$ is obtained where $E = 163$ GPa. The data of fracture energy density with respective standard deviation against the specimen volumes is plotted in Fig. 11 where size effect is clearly evident. The prediction with equation (18) is also plotted in Fig. 11 with coefficients $w_0 = 30$ MPa and $V_0 = 100$ μm^3 (the best fit). Again, a qualitatively satisfactory agreement with data establishes the general applicability of the proposed size effect law (18).



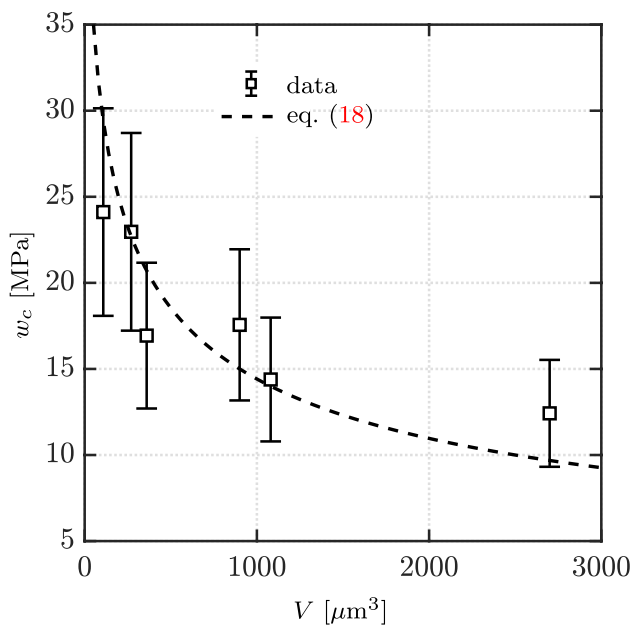


Fig. 11 Data of tensile testing with different sizes performed with nondoped polycrystalline silicon in Tsuchiya et al. [23]. The prediction with the proposed law (18) obtained with coefficients $w_0 = 30$ MPa and $V_0 = 100 \mu\text{m}^3$ is superimposed

Concluding Remarks

Lightweight intermetallic titanium aluminide alloys present promising thermo-mechanical properties for next generation of fuel efficient aero engines. However, due to their quasi-brittle response and complex microstructure, new theoretical and numerical methods need to be developed to perform precise computational design and analysis of TiAl components. In this work, three-point bending tests of geometrically identical TiAl specimens are performed and force displacement data and optically measured strain distributions are recorded. To analyze the data, theoretical and numerical formulation of ductile fracture is employed, which is based on the extension of phenomenological von Mises plasticity coupled to phase field method of fracture. Simulations are performed which reproduce data with very high accuracy. A critical fracture energy density for each of the tested specimen sizes is obtained directly from simulation results which show a dependence on the tested volume – so called *size effect*. A new empirical size effect law is proposed which relates the fracture energy density of the tested specimen with its volume. The fracture energy of an intermetallic TiAl alloy from a separate tensile test in literature is accurately predicted by the proposed size effect law. With only two physically motivated constants, the general applicability of the new size effect law is tested with different classes of quasi-brittle materials using data from literature and shows excellent predictive capabilities.

Acknowledgements The author acknowledges the support of Andreas Monden, Nora Schorer and Marco Korkisch at the University of Augsburg for the experimental testing and Sophie-Maria Rauscher at DLR for cleaning Aramis™ data.

Funding Information Open Access funding enabled and organized by Projekt DEAL. The research work was supported by the base funding of the institute provided by the Federal Ministry for Economic Affairs and Energy (BMWi).

Declarations

Conflict of Interest The author has no conflict of interest.

Open Access This article is licensed under a Creative Commons Attribution 4.0 International License, which permits use, sharing, adaptation, distribution and reproduction in any medium or format, as long as you give appropriate credit to the original author(s) and the source, provide a link to the Creative Commons licence, and indicate if changes were made. The images or other third party material in this article are included in the article's Creative Commons licence, unless indicated otherwise in a credit line to the material. If material is not included in the article's Creative Commons licence and your intended use is not permitted by statutory regulation or exceeds the permitted use, you will need to obtain permission directly from the copyright holder. To view a copy of this licence, visit <http://creativecommons.org/licenses/by/4.0/>.

References

- Horvath CD (2010) 2 - Advanced steels for lightweight automotive structures. In: Mallick PK (ed) Materials, Design and Manufacturing for Lightweight Vehicles, Woodhead Publishing, pp 35–78. <https://doi.org/10.1533/9781845697822.1.35>
- Rugg D (2014) Materials for future gas turbine applications. Mater Sci Technol 30(15):1848–1852. <https://doi.org/10.1179/1743284714Y.0000000609>
- Yvon P, Carré F (2009) Structural materials challenges for advanced reactor systems. J Nucl Mater 385(2):217–222. <https://doi.org/10.1016/j.jnucmat.2008.11.026>
- Squire TH, Marschall J (2010) Material property requirements for analysis and design of UHTC components in hypersonic applications. J Eur Ceram Soc 30(11):2239–2251. <https://doi.org/10.1016/j.jeurceramsoc.2010.01.026>
- Pollock TM (2016) Alloy design for aircraft engines. Nat Mater 15:809–815. <https://doi.org/10.1038/nmat4709>
- Appel F, Paul JDH, Oehring M (2011) Gamma titanium aluminide alloys: Science and Technology. Wiley-VCH Verlag & Co, KGaA, Germany
- Kim YW (1989) Intermetallic alloys based on gamma Titanium Aluminide. JOM 41(7):24–30. <https://doi.org/10.1007/BF03220267>
- Appel F, Wagner R (1998) Microstructure and deformation of two-phase γ -titanium aluminides. Mater Sci Eng R Rep 22(5):187–268. [https://doi.org/10.1016/S0927-796X\(97\)00018-1](https://doi.org/10.1016/S0927-796X(97)00018-1)
- Yao Z, Marek M (1995) NaCl-induced hot corrosion of a titanium aluminide alloy. Mater Sci Eng, A 192:994–1000. [https://doi.org/10.1016/0921-5093\(95\)03345-9](https://doi.org/10.1016/0921-5093(95)03345-9)
- Blackburn MJ, Smith MP (1981) Titanium alloys of the TiAl type. US Patent 4294615, <https://patents.google.com/patent/US4294615A/en?q=4294615>
- Schafrik RE (2016) Materials for a non-steady-state world. Metall Mater Trans A 47A:2539–2549. <https://doi.org/10.1007/s11661-016-3442-6>



12. Weibull W (1939) A statistical theory of the strength of materials. *Proc Royal Swedish Inst Eng Res* 151:1–45
13. Bažant ZP (1984) Size effect in blunt fracture: Concrete, rock, metal. *J Eng Mech* 110(4):518–535. [https://doi.org/10.1061/\(ASCE\)0733-9399\(1984\)110:4\(518\)](https://doi.org/10.1061/(ASCE)0733-9399(1984)110:4(518))
14. Bažant ZP, Le JL (2017) Probabilistic Mechanics of Quasibrittle Structures: Strength, Lifetime, and Size Effect. Cambridge University Press. <https://doi.org/10.1017/9781316585146>
15. Bažant ZP, Xi Y, Reid SG (1991) Statistical size effect in quasi-brittle structures: I. Is weibull theory applicable? *J Eng Mech* 117(11):2609–2622. [https://doi.org/10.1061/\(ASCE\)0733-9399\(1991\)117:11\(2609\)](https://doi.org/10.1061/(ASCE)0733-9399(1991)117:11(2609))
16. Hu X, Duan K (2008) Size effect and quasi-brittle fracture: the role of fpz. *Int J Fract* 154:3–14. <https://doi.org/10.1007/s10704-008-9290-7>
17. Yu Q, Le JL, Hoover CG, Bažant ZP (2010) Problems with Hu-Duan boundary effect model and its comparison to size-shape effect law for quasi-brittle fracture. *J Eng Mech* 136(1):40–50. [https://doi.org/10.1061/\(ASCE\)EM.1943-7889.89](https://doi.org/10.1061/(ASCE)EM.1943-7889.89)
18. Hu X, Guan J, Wang Y, Keating A, Yang S (2017) Comparison of boundary and size effect models based on new developments. *Eng Fract Mech* 175:146–167. <https://doi.org/10.1016/j.engfracmech.2017.02.005>
19. Hall EO (1951) The deformation and ageing of mild steel: III. discussion of results. *Proc Phys Soc B* 64:747–753. <https://doi.org/10.1088/0370-1301/64/9/303>
20. Petch NJ (1953) The cleavage strength of polycrystals. *J Iron Steel Inst* 174:25–28
21. Hansen N (2004) Hall-Petch relation and boundary strengthening. *Scr Mater* 51:801–806. <https://doi.org/10.1016/j.scriptamat.2004.06.002>
22. Fleck NA, Muller GM, Ashby MF, Hutchinson JW (1994) Strain gradient plasticity: Theory and experiment. *Acta Metall Mater* 42(2):475–487. [https://doi.org/10.1016/0956-7151\(94\)90502-9](https://doi.org/10.1016/0956-7151(94)90502-9)
23. Tsuchiya T, Tabata O, Sakata J, Taga Y (1998) Specimen size effect on tensile strength of surface-micromachined polycrystalline silicon thin films. *J Microelectromech Syst* 7(1):106–113. <https://doi.org/10.1109/84.661392>
24. Wallin K (2002) Master curve analysis of the Euro fracture toughness dataset. *Eng Fract Mech* 69:451–481. [https://doi.org/10.1016/S0013-7944\(01\)00071-6](https://doi.org/10.1016/S0013-7944(01)00071-6)
25. Greer JR, De Hosson JTM (2011) Plasticity in small-sized metallic systems: Intrinsic versus extrinsic size effect. *Prog Mater Sci* 56(6):654–724. <https://doi.org/10.1016/j.pmatsci.2011.01.005>
26. Bennett JA, Weinberg JG (1954) Fatigue notch sensitivity of some aluminum alloys. *J Res Nat Bur Stand* 52(5):235–245
27. Forrest PG (1962) *Fatigue of metals*, 1st edn. Pergamon Press Ltd., London
28. Lazzarin P, Tovo R, Meneghetti G (1997) Fatigue crack initiation and propagation phases near notches in metals with low notch sensitivity. *Int J Fatigue* 19(8–9):647–657. [https://doi.org/10.1016/S0142-1123\(97\)00091-1](https://doi.org/10.1016/S0142-1123(97)00091-1)
29. Sapora A, Cornetti P, Campagnolo A, Meneghetti G (2020) Fatigue limit: Crack and notch sensitivity by finite fracture mechanics. *Theor Appl Fract Mech* 105. <https://doi.org/10.1016/j.tafmec.2019.102407>
30. Karry RW, Dolan TJ (1953) Influence of grain size on fatigue notch-sensitivity. In: *ASTM Proceeding PRO1953-53*, vol 53, pp 789–804
31. Lukáš P, Kunz L, Svoboda M (2005) Fatigue notch sensitivity of ultrafine-grained copper. *Mater Sci Eng, A* 391(1–2):337–341. <https://doi.org/10.1016/j.msea.2004.09.052>
32. Furnish TA, Boyce BL, Sharon JA, O'Brien CJ (2016) Fatigue stress concentration and notch sensitivity in nanocrystalline metals. *J Mater Res* 31(6):740–752. <https://doi.org/10.1557/jmr.2016.66>
33. Berto F, Lazzarin P (2014) Recent developments in brittle and quasi-brittle failure assessment of engineering materials by means of local approaches. *Mater Sci Eng R Rep* 75:1–48. <https://doi.org/10.1016/j.mser.2013.11.001>
34. Anderson TL (2017) *Fracture mechanics: Fundamentals and Applications*, 4th edn. CRC Press, Boca Raton. <https://doi.org/10.1201/9781315370293>
35. Griffith AA (1920) The phenomena of rupture and flow in solids. *Phil Trans Series A* 221:163–198. <https://doi.org/10.1098/rsta.1921.0006>
36. Miehe C, Aldakheel F, Raina A (2016) Phase field modeling of ductile fracture at finite strains: a variational gradient-extended plasticity-damage theory. *Int J Plast* 84:1–32. <https://doi.org/10.1016/j.iplas.2016.04.011>
37. Raina A (2014) Multi-level descriptions of failure phenomena with the strong discontinuity approach. PhD thesis, University of Stuttgart
38. Linder C, Raina A (2013) A strong discontinuity approach on multiple levels to model solids at failure. *Comput Methods Appl Mech Eng* 253:558–583. <https://doi.org/10.1016/j.cma.2012.07.005>
39. Raina A, Miehe C (2015) A phase-field model for fracture in biological tissues. *Biomech Model Mechanobiol* 15(3):479–496. <https://doi.org/10.1007/s10237-015-0702-0>
40. Miehe C, Dal H, Schänzel LM, Raina A (2015) A phase-field model for chemo-mechanical induced fracture in lithium-ion battery electrode particles. *Int J Numer Methods Eng* 106(9):683–711. <https://doi.org/10.1002/nme.5133>
41. Borden MJ, Hughes TJ, Landis CM, Anvari A, Lee IJ (2016) A phase-field formulation for fracture in ductile materials: Finite deformation balance law derivation, plastic degradation, and stress triaxiality effects. *Comput Methods Appl Mech Eng* 312:130–166. <https://doi.org/10.1016/j.cma.2016.09.005>
42. Miehe C (2011) A multi-field incremental variational framework for gradient-extended standard dissipative solids. *J Mech Phys Solids* 59(4):898–923. <https://doi.org/10.1016/j.jmps.2010.11.001>
43. Dugdale DS (1960) Yielding in steel sheets containing slits. *J Mech Phys Solids* 8(2):100–104. [https://doi.org/10.1016/0022-5096\(60\)90013-2](https://doi.org/10.1016/0022-5096(60)90013-2)
44. Barenblatt GI (1962) The mathematical theory of equilibrium cracks in brittle fracture. *Adv Appl Mech* 7:55–129. [https://doi.org/10.1016/S0065-2156\(08\)70121-2](https://doi.org/10.1016/S0065-2156(08)70121-2)
45. Irwin GR (1961) Plastic zone near a crack and fracture toughness. *Sagamore Research Conference Proceedings*, vol 4. Syracuse University Research Institute, Syracuse NY, pp 63–78
46. Dresbach C, Becker T et al (2016) A stochastic reliability model for application in a multidisciplinary optimization of a low pressure turbine blade made of titanium aluminide. *Lat Am J Solids Struct* 13:2316–2332. <https://doi.org/10.1590/1679-78252521>
47. Zok FW (2017) On weakest link theory and weibull statistics. *J Am Ceram Soc* 100(4):1265–1268. <https://doi.org/10.1111/jace.14665>
48. Hoover CG, Bazant ZP, Vorel J, Wendner R, Hubler MH (2013) Comprehensive concrete fracture tests: Description and results. *Eng Fract Mech* 114:92–103. <https://doi.org/10.1016/j.engfracmech.2013.08.007>
49. Narayan S, Anand L (2019) A gradient-damage theory for fracture of quasi-brittle materials. *J Mech Phys Solids* 129:119–146. <https://doi.org/10.1016/j.jmps.2019.05.001>

